Hydride Doping Effects on the Structure and Properties of Eight-Electron Rh/Ag Superatoms: The [RhH x @Ag 21-x S 2 P(O n Pr) 2 12] (x = 0-2) Series

Tzu-Hao Chiu, Jian-Hong Liao, Ying-Yann Wu, Jie-Ying Chen, Yuan Jang Chen, Xiaoping Wang, Samia Kahlal, Jean- Yves Saillard, C W Liu

Hydride Doping Effects on the Structure and Properties of Eight-Electron Rh/Ag *Superatoms: The [$RhH_x@Ag_{21-x}\{S_2P(O^nPr)_2\}_{12}$] (x = 0-2) Series*

Tzu-Hao Chiu,[a] Jian-Hong Liao,[a] Ying-Yann Wu,[a] Jie-Ying Chen,[b] Yuan Jang Chen,[b] Xiaoping Wang,[c] Samia Kahlal,[d] Jean-Yves Saillard,[d]* and C. W. Liu[a]*

[a] *Department of Chemistry, National Dong Hwa University, Hualien 97401, Taiwan (Republic of China)*

[b] *Department of Chemistry, Fu-Jen Catholic University, New Taipei City 24205, Taiwan (Republic of China)*

[c] *Neutron Scattering Division, Neutron Sciences Directorate, Oak Ridge National Laboratory, Oak Ridge, TN 37831, U.S.A.*

[d] *Univ Rennes, CNRS, ISCR-UMR 6226, F-35000 Rennes, France*

*Correspondence: E-mail: chenwei@gms.ndhu.edu.tw; Tel: +886-3-890-3607; Fax: +886-3-890-0162; http://faculty.ndhu.edu.tw/~cwl/index.htm

Keywords: Rhodium, Silver, Hydride, Neutron diffraction, Superatomic alloys

ABSTRACT: Three hitherto unknown eight-electron rhodium/silver alloy nanoclusters, $[RhAg_{21}\{S_2P(O^nPr)_2\}_{12}]$ (**1**), $[RhHAg_{20}\{S_2P(O^nPr)_2\}_{12}]$ (**2**) and $[RhH_2Ag_{19}\{S_2P(O^nPr)_2\}_{12}]$ (**3**), have been isolated and fully characterized. Cluster **1** contains a regular $Rh@Ag_{12}$ icosahedral core, whereas **2** and **3** exhibit distorted $RhH@Ag_{12}$ and $RhH_2@Ag_{12}$ icosahedral cores. The single-crystal neutron structure of **2** located the encapsulated hydride sitting at the center of an enlarged $RhAg_3$ tetrahedron. A similar position was found by neutron diffraction for one of the hydrides in **3**, whereas the other hydride is trigonally coordinated to Rh and an elongated Ag-Ag edge. The solid-state structures of **1**-**3** possess C_1 symmetry due to the asymmetric arrangement of the surrounding capping Ag atoms. Our investigation shows that the insertion of one hydride dopant provokes the elimination of one capping silver atom on the cluster surface, resulting in the general formula $[RhH_x@Ag_{21-x}\{S_2P(O^nPr)_2\}_{12}]$ (x = 0-2), which maintains the same number of cluster electrons as well as neutral charge. Clusters **1**-**3** exhibit an intense emission band in the NIR region. Contrarily to their $PdAg_{21}$ and $PdHAg_{20}$ relatives, the 4d orbitals of the encapsulated heterometal are somewhat involved in the optical processes.

Introduction

Ligand-protected nanoclusters (NCs) with precise atomic and geometric arrangements have gained attentions owing to their unique physicochemical properties.[1-5] Their electronic structures, whose shapes are reminiscent of the conventional atomic orbitals, can be conceptualized by the *superatom* model.[6] Following the discovery of several stable 8-electron *superatoms*,[7-12] altering the physicochemical properties of clusters through heterometal doping has become a topical research project in recent years.[13-30] One of the broadly studied targets, the centered icosahedral $[Au_{13}]^{5+}$,[7] which is protected by diphosphines and halides, has successfully been doped by Group 8 ~ 10 metals at its center,[26-29] maintaining the 8-electron count, and there is evidence that the dopant significantly affects the photophysical properties.[28-29] Interestingly, when doping the thiolate-protected $[Ag_{25}]^{17+}$ framework with a Group 9 metal,[14] the actual dopant is MH, not M (M= Rh or Ir). Very recently, the same group shown that when using a Group 8 metal, the actual dopant is MH_2 (M = Ru, Os).[15] The anisotropic distortion resulting from the presence of more than one atom at the center of the icosahedral core prevents it from being a useful reference for metric data comparison with $M@Ag_{24}$ (M=Ag,[10] Au,[23] Ni,[21] Pd,[22] Pt[22]). Additionally, the presence of an additional hydride inside the icosahedral cage may make the NCs to behave differently. For instance, $PdAg_{20}[S_2P(OR)_2]_{12}$ displays remarkable photoluminescence at 77K, whereas $[PdHAg_{20}\{S_2P(OR)_2\}_{12}]^+$ does not exhibit any photoluminescence even at the same temperature.[30-31] Therefore, preparation of Rh-doped silver *superatoms* is essential for the comparison of doping effects.

To obtain mixed-valence metal NCs, reducing agents are often added during the synthesis. In many cases, BH_4^- is most commonly used for group 11 metal-based NCs. It is a provider of hydrides (H^-), which have played a significant role in the reduction-derived nanoparticle synthesis.[13-15, 32-33] Hydrides can act as reducing agents, but also can behave as ligands, their very small size allowing them to occupy interstitial positions inside the metal kernel. We have recently shown that interstitial hydrides connected to noble metals, whose electronegativity values are larger than H, exhibit properties that differ from those of conventional ligands.[13, 31] Therefore, accurately identifying the hydride

position is important, as hydrides may exhibit different properties at different positions. Also, an interesting question is: can an icosahedral cage encapsulate several hydrides and does the amount of hydrides affects the electronic structure and photophysical properties? Here, we report three new 8-electron Rh/Ag *superatomic* alloys, **1**, **2**, and **3**, containing different amounts of hydrides. The dopants for **1**, **2**, and **3** are Rh, RhH, and RhH_2, respectively. The results show that the degree of distortion of the $RhAg_{12}$ core increases upon increasing the amount of hydride dopant. The DFT calculations indicate that all three NCs are 8-electron *superatoms, the electrons of the encapsulated H atoms being part of this count*. The absorption spectrum shows a slightly blue-shifted signal upon replacing the dopant from Rh to RhH and RhH_2. *Notably, compound **1** is the first structurally characterized example of a hydride-free Rh-doped silver-rich superatom. Compounds **2** and **3** contain one and two hydrides in the Rh-doped silver-rich superatoms, and the hydride locations have been determined by neutron diffraction for the first time.*

Results and discussion

We have reported the syntheses of several ligand-protected NCs doped with group 10 metals, including $[MAg_{20}(dtp/dsep)_{12}]$ (M = Pd,[16] Pt[17]; dtp = dithiophosphate, dsep = diselenophosphate) and $[MHAg_{19}(dtp/dsep)_{12}]$ (M = Pd,[31] Pt[13]), using a one-pot co-reduction approach. In this study, three Rh-doped silver-rich NCs were obtained by co-reduction of $(NH_4)[S_2P(O^nPr)_2]$, $[Ag(MeCN)_4](PF_6)$, $[Rh(COD)Cl]_2$, and $NaBH_4$ in a molar ratio of $Ag^+/Rh^+/[S_2P(O^nPr)_2]^-/H^-$ of 20:1:10:20 (Scheme 1). The resulting three NCs can be separated by thin layer chromatography using an eluent composed of ether and hexane in

Scheme 1. The syntheses of **1-3**.

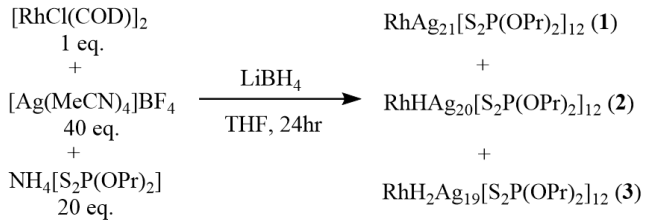

a 1:4 ratio (Figure S24). Single crystals of **1** and **2** can be obtained by evaporating MeOH solutions at 4°C within a week, while single crystals of **3** by diffusing *n*-hexane into methanol at 4°C in one week.

Compositions of **1**, **2**, and **3** were determined by positive-mode ESI mass spectrometry. The most intense band at 5035.8 Da corresponds to $[\mathbf{1}+Ag^+]^+$ (calc. 5036.0 Da, Figure 1a). In the spectra of **2** (Figure 1b) and $\mathbf{2_D}$ (Figure S1), the ion peaks at 4927.1 Da and 4928.1Da correspond to $[\mathbf{2}+Ag^+]^+$ (calc. 4927.1 Da) and $[\mathbf{2_D}+Ag^+]^+$ (calc. 4928.1 Da), respectively. For **3** (Figure 1c) and $\mathbf{3_D}$ (Figure S2), intense bands at m/z 4821.4 Da and 4823.4 are the adduct ions $[\mathbf{3}+Ag^+]^+$ (calc. 4821.2 Da) and $[\mathbf{3_D}+Ag^+]^+$ (calc. 4823.2 Da), respectively. Their simulated isotopic patterns match well with the experimental observations for all the NCs.

The single-crystal X-ray structures of **1**-**3** and the neutron structures of **2** and **3** ($\mathbf{2_N}$ and $\mathbf{3_N}$) are all consistent

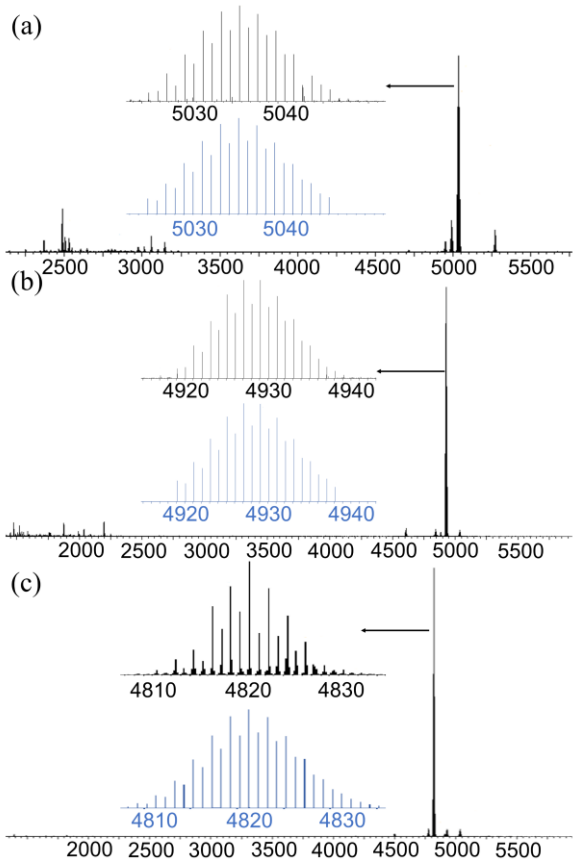

Figure 1. (a) Positive-mode ESI mass spectrum of **1**. Insets: experimental (top) and simulated (down) isotopic distribution of the ion peak $[\mathbf{1}+Ag^+]^+$. (b) Positive-mode ESI mass spectrum of **2**. Insets: experimental (top) and simulated (down) isotopic distribution of the ion peak $[\mathbf{2}+Ag^+]^+$(c) Positive-mode ESI mass spectrum of **3**. Insets: experimental (top) and simulated (down) isotopic distribution of the ion peak $[\mathbf{3}+Ag^+]^+$

with a general description featuring an Ag_{12} icosahedral core centered by a Rh, RhH and RhH_2 unit for clusters **1**, **2** and **3**, respectively (Figure 2a). This centered icosahedral core is protected by an outer shell made of 12 dtp ligands and 9, 8 and 7 capping Ag, atoms, respectively. Therefore, a general formula for these structures is $[RhH_x@(Ag_{ico})_{12}(Ag_{cap})_{9-x}(dtp)_{12}]^0$ (x = 0, 1 and 2 for **1**, **2** and **3**, respectively). Although the nuclearity and the number of ligands in $[RhAg_{21}(dtp)_{12}]$ (**1**) are the same as in $[Ag_{22}(dpa)_{12}]^{2+}$ (dpa = dipyridylamido),[34] the arrangement of the outer nine Ag_{cap} atoms differs, likely due to the use of different ligands. A similar 8-e alloy, $[PdAg_{21}(dtp)_{12}]^+$,[31] synthesized by adding an extra capping Ag atom onto a vacant triangular face of $[PdAg_{20}(dtp)_{12}]$, also features a slightly different arrangement from that in **1**. This difference may be due to different synthetic methods. Compound $[RhHAg_{20}(dtp)_{12}]$ (**2**) contains one interstitial H atom within the icosahedral core, whereas cluster **3** ($[RhH_2Ag_{19}(dtp)_{12}]$) contains two interstitial H atoms. Looking first at the three X-ray structures, one can see that the thirty icosahedron edges ($Ag_{ico}\cdots Ag_{ico}$) in **1**, (Figure 2b) fall within a narrow range of 2.8301(13) – 2.9683(14) Å

(avg. 2.8849(13) Å). Conversely, the $Ag_{ico}\cdots Ag_{ico}$ distances in **2** and **3** fall within larger ranges and are longer in average: 2.7949(7)-3.3981(6) Å (avg. 2.9230(7) Å) and 2.8162(11)-3.607(1) Å (avg. 2.945(1) Å), for **2** and **3** respectively. This elongation tendency is also visible in the Rh-Ag_{ico} distances (avg. 2.7368(13) Å in **1**, 2.7795(6) Å in **2**, and 2.8214(11) Å in **3**), as well as in the neutron structures of **2** (**2N**, see Figure 2c) and **3** (**3N**, see Figure 2d). The deviation from ideal I_h symmetry of a given icosahedron can be quantified by its continuous symmetry measure (CSM).[35] The Rh-centered Ag_{12} icosahedron in **1** has a small CSM value (0.04), close to that of an ideal icosahedron (CSM = 0) and similar to those of related species having $M@Ag_{12}$ cores (M = Pd,[16,30] Pt,[17] Au,[19-20,23] Ag[9-10,20,36]). The RhH-centered icosahedron has larger CSM values (0.15 (X-ray) and 0.24 (neutron), respectively), similar to those in $[PtHAg_{19}\{E_2P(O^nPr)_2\}_{12}]$ (E = S, 0.16; E = Se, 0.15),[13] in $[PdH@Ag_{19}\{S_2P(O^iPr)_2\}_{12}]$ (0.22),[31] in $[PdH@Ag_{19}\{S_2P(O^iPr)_2\}_{12}]$ (0.14),[31] and in $[RhHAg_{24}(SPhMe_2)_{18}]^{2-}$ (0.27),[14] but slightly smaller than that in $[IrHAg_{24}(SPhMe_2)_{18}]^{2-}$ (0.35).[15] The RhH_2-centered icosahedron in **3** has an even larger CSM (0.43), which close to those in $[RuH_2Ag_{24}(SPhMe_2)_{18}]^{2-}$ (0.40) and $[OsH_2Ag_{24}(SPhMe_2)_{18}]^{2-}$ (0.32),[15] while that in **3N** is somewhat lower (0.26).

The existence of specifically elongated $Ag_{ico}\cdots Ag_{ico}$ distances in the X-ray structures of **2** and **3** (Figure S3) provides insight into the location of the interstitial hydrides. In structure **2** (Figure S3a), the long Ag9-Ag10, Ag4-Ag10, and Ag4-Ag9 distances (3.3981(6) Å, 3.3323(7) Å, and 3.0151(7) Å, respectively), featuring an expanded Ag4-Ag9-Ag10 triangular face and indicating that the hydride is most likely to be found located within the enlarged Rh-Ag4-Ag9-Ag10 tetrahedron, a correlation previously noted in the other H-containing Ag NCs $[PtH@Ag_{19}\{E_2P(O^nPr)_2\}_{12}]$ (E = S, Se),[13] $[PdH@Ag_{19}\{S_2P(O^iPr)_2\}_{12}]$,[31] $[PdHAg_{20}\{S_2P(O^iPr)_2\}_{12}]^+$,[31] and $[RhH@Ag_{24}(SPhMe_2)_{18}]^{2-}$.[14] As a matter of fact, this is the H1M hydride position that was suggested from the residual electron density map in the X-ray structure of **2**, and subsequently refined to convergence without constraints. This position was further validated unambiguously by single-crystal neutron diffraction. Indeed, structure **2N** reveals a nuclear density map with only one negative peak, corresponding to a hydride, and tetrahedrally connected to Ag4, Ag9, and Ag10 and Rh, as illustrated in Figure 2e. The Rh-H distance in **2N** is 1.616(11) Å, with the average Ag_{ico}-H distance at 1.966(15) Å. It is worth noting that these values closely resemble those of the X-ray structure of **2**, where the Rh-H distance and average Ag_{ico}-H distance were found to be 1.59(7) Å and 1.97(7) Å, respectively. These findings indicate that the hydride position identified from the high-resolution X-ray data is fully consistent with that validated from neutron data.

Upon analyzing the X-ray structure **3**, a relatively large number of $Ag_{ico}\cdots Ag_{ico}$ distances exceeding 3.0 Å were observed (Table S1 and Figure S3b), when compared with structure **2**. This includes those within the Ag2-Ag6-Ag7 triangle (3.228(1) Å - 3.369(1) Å), as well as the Ag5…Ag11 distance (3.607(1) Å). Based on the above examples, it can be speculated that the hydride positions should be connected to the longer edges of the icosahedron. Indeed, the residual electron density map in the X-ray structure of **3** suggested such positions which were later precisely authenticated by neutron diffraction (structure **3N**, Figure 2d). H1M connects with the central Rh and the Ag5-Ag11 edge, resulting in a three-coordinated trigonal-planar geometry. H2M connects with Rh and the Ag2-Ag6-Ag7 triangle, forming a distorted tetrahedral geometry (Figure 2f). The distances between H1M and Ag6 or H1M and Ag10 in **3N** are longer than 2.2 Å, and thus are not considered as bonding (Figure S4). The Ag_{ico}-H1M distances are 1.65(7) Å and 2.02(7) Å, while the Ag_{ico}-H2M distances range from 1.72(8) to 2.02(8) Å (avg. 1.85(8) Å). The Rh-H distances in

Table 1. Selected experimental bond distances (Å) and angles (deg.) for **1**, **2**, **2N**, **3** and **3N**, and their DFT-optimized counterparts.

Comp.	**1** (X-ray)	**1** (DFT)	**2** (X-ray)	**2N** (neutron)	**2** (DFT)	**3** (X-ray)	**3N** (neutron)	**3** (DFT)
CSM	0.04	0.05	0.15	0.24	0.24	0.43	0.26	0.46
Rh–Ag_{ico}	2.6871(12)–2.8028(14) avg. 2.7368(13)	2.771–2.901 avg. 2.832	2.7298(7)–2.8981(7) avg. 2.7795(6)	2.725(9)–2.886(7) avg. 2.776(8)	2.832–3.022 avg. 2.872	2.7477(11)–2.9414(11) avg. 2.8214(11)	2.72(4)–2.90(5) avg. 2.82(5)	2.828–3.099 avg. 2.916
Ag_{ico}–Ag_{ico}	2.8301(13)–2.9683(14) avg. 2.8849(13)	2.908–3.088 avg. 2.978	2.7949(7)–3.3981(6) avg. 2.9230(7)	2.781(8) – 3.414(8) avg. 2.919(8)	2.896–3.171 avg. 2.987	2.8162(11)–3.3689(14) avg. 2.9450(12)	2.79(5)–3.51(5) avg. 2.94(5)	2.912–3.666 avg. 3.065
Ag_{ico}–Ag_{cap}	2.804(2)–3.1068(13) avg. 2.935(2)	2.942–3.360 avg. 3.068	2.8924(7)–3.1250(7) avg. 2.9817(4)	2.902(8)–3.137(8) avg. 2.990(8)	2.974–3.289 avg. 3.104	2.9283(11)–3.1337(13) avg. 3.0221(11)	2.91(4)–3.15(5) avg. 3.02(5)	3.015–3.295 avg. 3.143
Rh–H	–	–	1.59(7)	1.616(11)	1.658	1.6853 (7)–1.7139(8) avg. 1.6996 (8)	1.72(8)–1.76(6) avg. 1.74(7)	1.663–1.666 avg. 1.665
Ag_{ico}–H	–		1.86(7)–2.11(7) avg. 1.97(7)	1.860(13)–2.089(16) avg. 1.966(15)	1.934–2.108 avg. 2.039	1.7471 (8)–2.1823(8) avg. 1.9803 (9)	1.65(7)–2.02(8) avg. 1.84(8)	1.949–2.192 avg. 2.067
H–Rh–H	–		–	–		100.57(4)	101(4)	81

3N are 1.72(8) Å and 1.76(6) Å. The H1M-Rh1-H2M angle measures 101(4)° and the distance between H1M and H2M is 2.7(1) Å, indicating non-interacting hydrides.

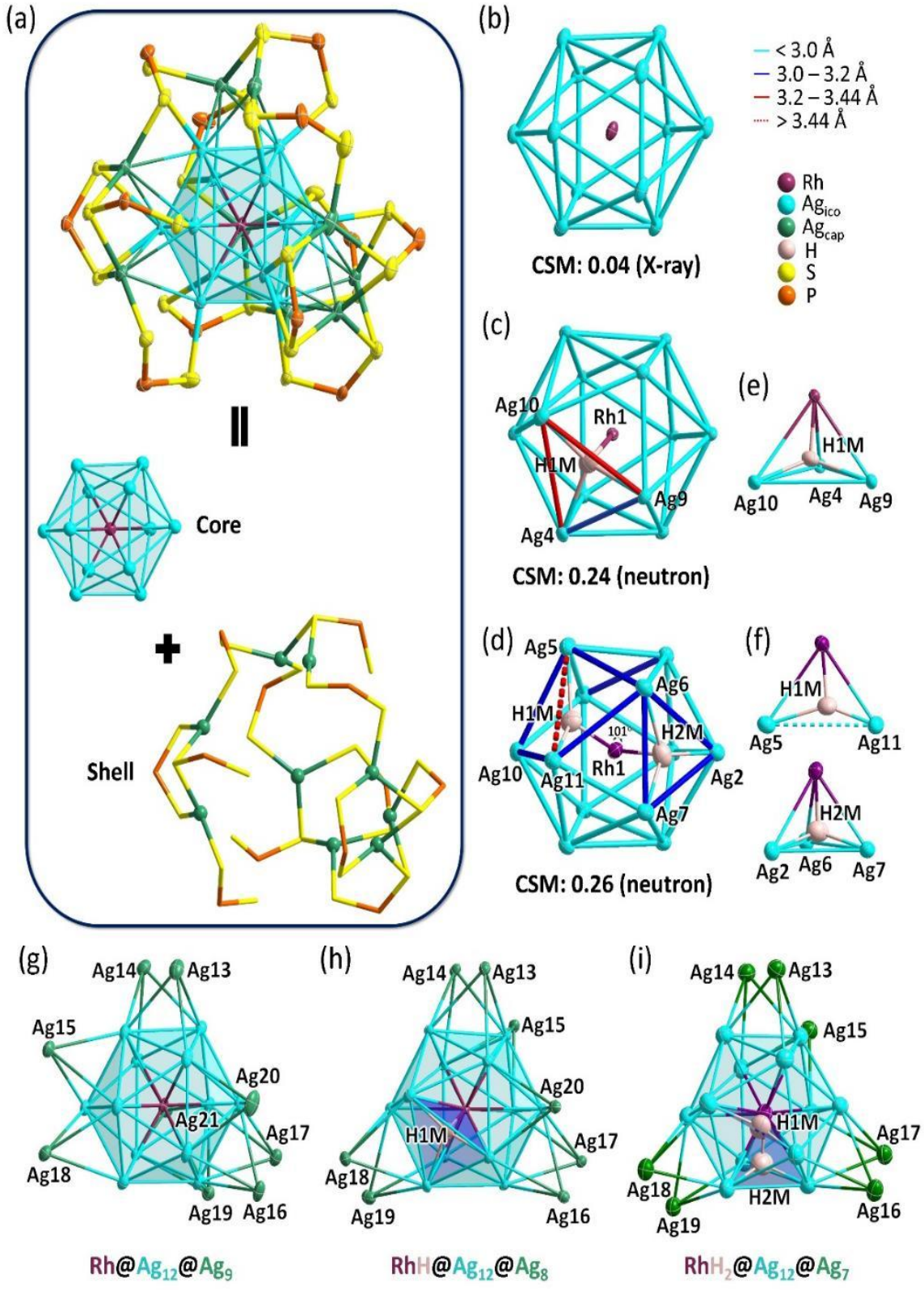

Figure 2. (a) Total structure of **1** and disassembly diagram of its *superatomic* core and shell. (b) $Rh@Ag_{12}$ icosahedral core of **1**. (c) $RhH@Ag_{12}$ icosahedral core in **2N** (neutron data) and (d) $RhH_2@Ag_{12}$ icosahedral core in **3N** (neutron data). (e) The coordination environment of the hydride in **2N**. (f) The coordination environment of the two hydrides in **3N**. (g) $RhAg_{21}$ core of **1** (X-ray data, major contribution). (h) $RhHAg_{20}$ core of **2N**. (i) RhH_2Ag_{19} core of **3N**.

Structures **1**-**3** possess C_1 symmetry due to the asymmetric arrangement of their capping atoms. It is of note that the structure of **1** is the second example of a dithiolate-protected NC with nine-capping Ag atoms.[31] The topology of the eight outer Ag_{cap} in **2** (C_1) is different from those more symmetric encountered in $AuAg_{20}$ (T_h),[19] Ag_{21} (D_3)[9] and $PtAg_{20}$ (C_2).[17] The seven Ag_{cap} in **3** arrange in a similar way as in the isoelectronic $[Ag_{20}\{S_2P(O^nPr)_2\}_{12}]$.[36] The orientation of the 12 ligands in **1** differs significantly from that in **2**, while the ligands in **2** and **3** exhibit high similarity (Figure S6). A common feature to the hydride-connected triangular faces in **2** and **3** is that they are not bridged by dtp ligands. This lack of bridging ligands likely contributes to the elongation of the $Ag_{ico}\cdots Ag_{ico}$ distance, which in turn makes hydrides more likely to stay at these positions (Figure S6d). The $Ag_{ico}\cdots Ag_{cap}$ distances (2.804(2) – 3.1068(13) Å in **1**, 2.8924(7) – 3.1250(7) Å in **2**, and 2.9283(11) – 3.1337(13) Å in **3**) indicate relatively weak argentophilic interactions, in agreement with the fluxional behavior of the surface Ag_{cap} atoms in solution (see below). This might also explain the common disorder of capping atoms in the crystal structures of **1**-**3**, leading to the formation of structural isomers. For example, in structure **1**, Ag13 and Ag21 are major contributions (75%), while Ag22 and Ag23 are minor contributions (25%, see Figure S5). Only the structures with major contributions are discussed above.

The ambient temperature $^{31}P\{^1H\}$ NMR spectra of compounds **1**, **2** and **3** exhibit a single sharp peak at 102.4 ppm, 104.1 ppm and 105.3 ppm, respectively. The ^{31}P resonance frequency shifts up-field with an increase in the total number of metal atoms. In the VT $^{31}P\{^1H\}$ NMR spectrum of **1** (Figure S12), the sharp resonance at 102.4 ppm at 293K can be resolved into more than twelve peaks at 173K, indicating the presence of several C_1 isomers. No hydride peak can be identified in the ^1H NMR spectrum of **1** (Figure S7). In contrast, the room temperature ^1H spectra of **2** and **3** display a broad peak centered at -13.7 ppm (Figure S8) and -13.6 ppm (Figure S9), respectively. The ^2H NMR spectra of their deuterated analogs $\mathbf{2_D}$ and $\mathbf{3_D}$ show deuteride resonances at -13.7 (Figure S10) and -13.6 ppm (Figure S11), respectively. Similarly, to the VT $^{31}P\{^1H\}$ NMR spectrum of **1**, the ^{31}P resonance of **2** gradually splits into more than twelve peaks at 163K (Figure S13), and its ^1H NMR spectrum at 163K shows two major unresolved peaks centered at -13.0 and -14.1 ppm (Figure S14). These VT NMR spectra suggest the presence of isomers of different symmetries in solution, as those previously observed in $[PtHAg_{19}\{S_2P(O^nPr)_2\}_{12}]$.[13] In comparison, the hydride resonance of **3** does not split into several peaks at low temperature but remains as a broad peak at 163K (Figure S16). *This observation strongly suggests rapid atomic movements of the two interstitial hydrides, swapping between tetrahedral cavities within the* $RhAg_{12}$ *kernel.* This phenomenon may give a hint of the failure to detect any scalar coupling between the hydride and peripheral NMR active nuclei such as ^{109}Ag and ^{103}Rh.

Thermal stability of the three compounds was evaluated by monitoring the time-dependent $^{31}P\{^1H\}$ NMR spectra of each compound in an NMR tube after heating them to 60℃. Compounds **1** (Figure S17) and **2** (Figure S18) display excellent thermal stability, with no changes observed in their resonances, even after three days. In contrast, compound **3** gradually transforms into **2** within 6 hours under the same conditions (Figure S19-S20). This suggests that one of the hydrides in **3** tends to dissociate as H^+ at 60℃, with concomitant trapping of one additional capping Ag^+, leading to the formation of the neutral cluster **2**. Notably, no other counter-cation is present in the solution to generate the hypothetical $[RhHAg_{19}(dtp)_{12}]^-$. The additional Ag^+ ions are likely generated by the decomposition of **3** under thermal conditions. Once **3** is fully transformed into **2**, no further changes occur.

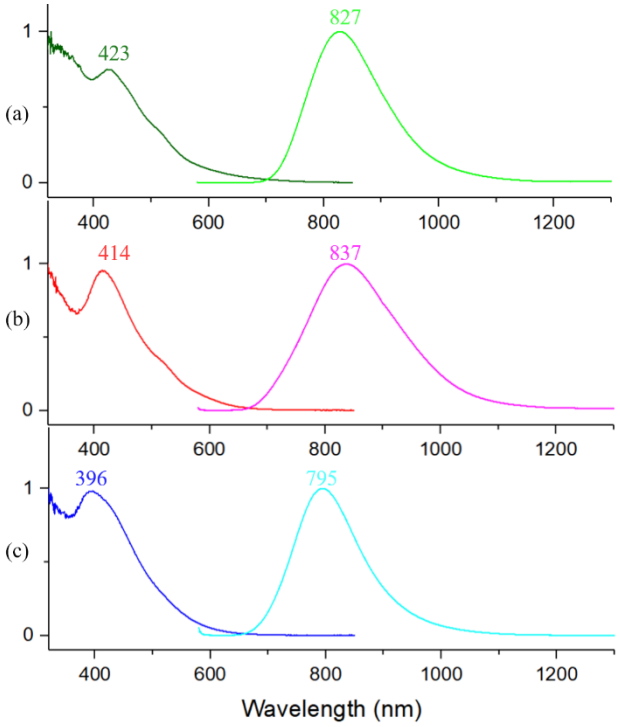

Figure 3. (a) Absorption (green) and emission (light green, 2-MeTHF glass, 77K) spectrum of **1**. (b) Absorption (red) and emission (pink, 2-MeTHF glass, 77K) spectrum of **2**. (c) Absorption (blue) and emission (light blue, 2-MeTHF glass, 77K) spectrum of **3**.

The UV-vis absorption spectrum (Figure 3) shows one intense band centered at 423 nm in **1**, 414 nm in **2**, and 396 nm in **3**, respectively. The photoluminescence (PL) spectra of **1**-**3** exhibit an intense emission in the NIR region at 827 (**1**), 837 (**2**), and 795 nm (**3**). The optical properties can be altered in various ways, such as surface modification, changing dopants, altering the electronic structure of the *superatomic* core, etc. To understand the effects of hydride doping in *superatom*, we focus on two different systems, MAg_{21} and $MHAg_{20}$ (M = Pd or Rh). The absorption and photoluminescence spectra of **1** show a slight blue shift compared to $PdAg_{21}$ (UV-vis: 445nm; Emission: 842nm),[31] indicating that replacing the dopant with an

element on the left side of the same period tends to increase the cluster HOMO-LUMO gap, leading to a blue shift in both spectra. Similar blue shift phenomena are also observed in $PtAg_{20}$[17] and $AuAg_{20}$.[37] However, in the case of $MH@Ag_{20}$ (M=Rh or Pd), the opposite is observed, with the absorption spectrum of **2** showing a slight red shift compared to $PdHAg_{20}$ (UV-vis: 405nm).[31] This suggests that the doping of hydrides not only distorts the icosahedron, but also has a significant impact on the photophysical properties of the system. The PL decay curve of **1**-**3** (Figure S22) shows single exponential decay, corresponding to a single lifetime at 45 μs (**1**), 40 μs (**2**), and 64 μs (**3**), suggesting phosphorescence.

DFT investigations at the BP86/Def2-TZVP level were performed on compounds **1**-**3** (see Computational Details in the SI). For the sake of computational limitations, the $S_2P(O^nPr)_2$ ligands were replaced by S_2PH_2, a simplification that has been proven reasonable in many previous investigations.[9,13,16-20,30,31,36,37,40,42] Selected computed data are given in Tables 1 and 2. The computed metrics for **1** and **2** (Table 1) are in good agreement with their experimental counterparts, with a small overestimation of bond distances. In the case of **3**, the optimized and experimental structures do not match perfectly with respect to the hydride positions. This difference will be commented on later. The Ag_{cap} NBO charges (~ +0.7) are indicative of a +I oxidation state (Table 2),[9,13] which is consistent with the trigonal-planar (16-electron) or linear (14-electron) coordination of these metal centers (argentophilic contacts not considered). The substantially lower Ag_{ico} charges (~ +0.3/+0.4) indicate mixed-valent character. The hydride NBO charges in **2** and **3** (~ -0.3) approach that of their counterpart in $[PtHAg_{19}(dtp/dsep)_{12}]$.[13] This charge distribution, together with the significant Rh-Ag_{ico} Wiberg bond indices (WBIs) and the non-negligible Ag_{ico}-Ag_{ico} WBIs (larger than the mainly argentophilic Ag_{ico}-Ag_{cap} ones) are consistent with the view of **1**, **2** and **3** being made of 8-electron centered-icosahedral $[Rh@Ag_{12}]^{3+}$, $[RhH@Ag_{12}]^{4+}$, and $[RhH_2@Ag_{12}]^{5+}$ cores stabilized by 12 dtp^- and 9, 8, and 7 Ag^+ centers, respectively.[9,13,16-19,29,32,35,36] The Kohn-Sham orbital diagrams of the three NCs (Figures 4 and S29-S31) support this view, with their three highest occupied orbitals that can be identified as the 1P *superatomic* orbitals and their five lowest vacant ones as the 1D levels, a situation corresponding to the expected $1S^2$ $1P^6$ $1D^0$ *superatomic* closed-shell configuration.[6] Due to the presence of one and two encapsulated hydrides in **2** and **3**, respectively, the *superatomic* orbitals are respectively axially and planarly distorted away from regular spherical symmetry. Nevertheless, the HOMO-LUMO gaps of **2** and **3** are maintained even larger than that of **1** and no alternative electron count different from 8 is favored. The 1s(H) participation to the 1P and 1D *superatomic* orbitals in **2** and **3** is very small (Figure 4), in accordance with the rather small computed Ag-H Wiberg bond indices (Table 2). Calculations on the 8-electron cores of **2** and **3**, namely $[RhHAg_{12}]^{4+}$ and $[RhH_2Ag_{12}]^{5+}$ provided charge distributions and Wiberg indices that are consistent with those computed for **2** and **3** (Table 2), thus supporting the *superatomic* description of the latter cases. Due to substantial orbital mixing, it was not possible to identify a pure enough 1S orbital for clusters **1**-**3**. On the other hand, in the case of **2** and **3**, one and two, respectively, orbitals of

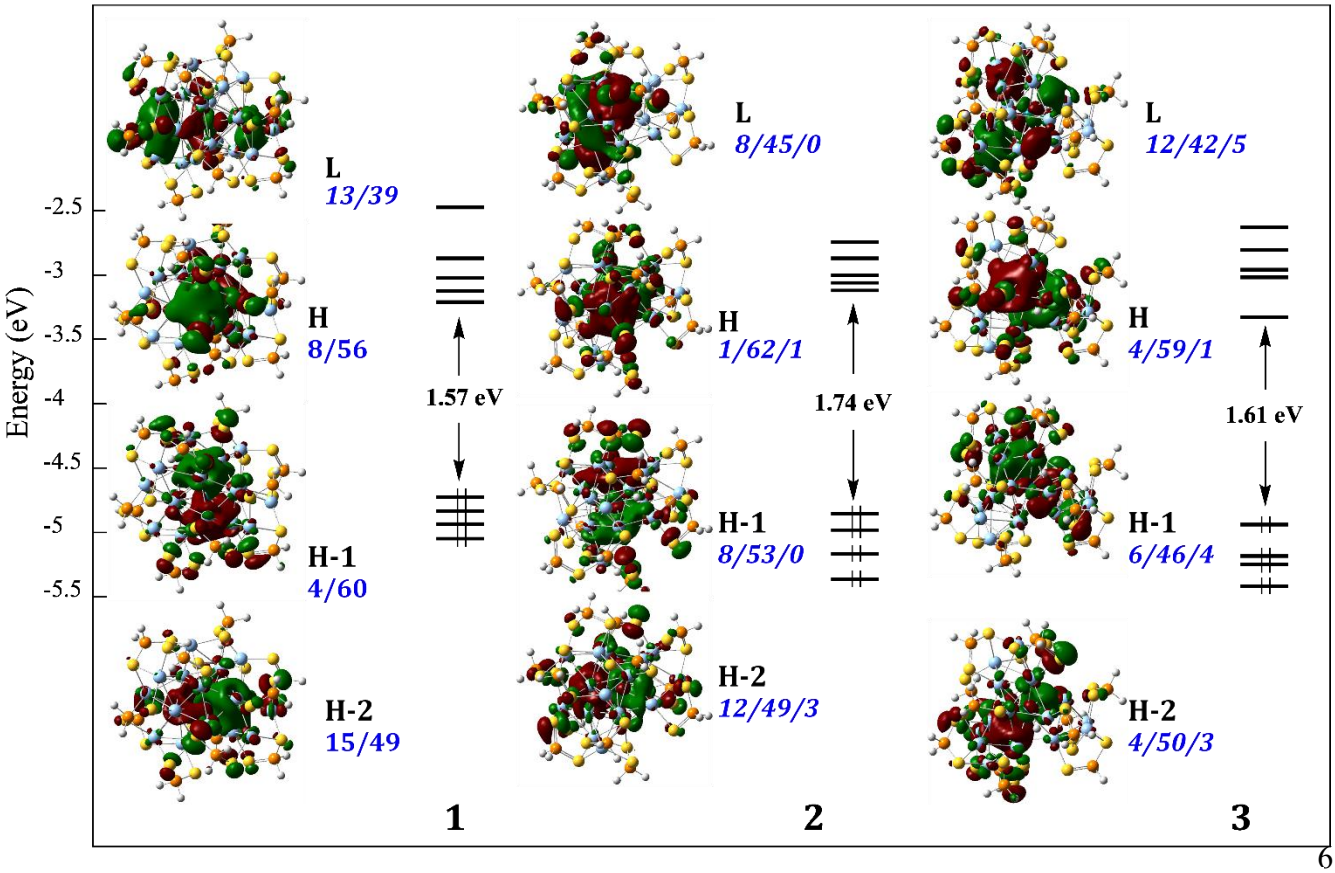

Figure 4. Kohn-Sham frontier orbital diagram of clusters **1**-**3** (H = HOMO; L = LUMO). Values in blue are the contribution (in %) of the core atoms or atom groups in the following order: $Rh/Ag_{12}/H_x$ (x = 1, 2).

Table 2. Selected DFT-computed data.

		$[RhHAg_{12}]^{4+}$	$[RhH_2Ag_{12}]^{5+}$	**1**	**2**	**3**
HOMO-LUMO gap (eV)		2.52	2.78	1.57	1.74	1.61
NAO charges	Rh	-2.10	-1.89	-1.67	-1.53	-1.40
	H	-0.36	-0.39	-	-0.34	-0.33
	RhH_x (x=0-2)	-2.46	-2.68	-1.67	-1.87	-2.05
	Ag_{ico} (av.)	+0.54	+0.64	+0.27	+0.33	+0.40
	Ag_{cap} (av.)			+0.68	+0.70	+0.70
Wiberg bond indices	Rh–H (av.)	0.257	0.230	-	0.240	0.235
	Ag–H (av.)	0.123	0.111	-	0.096	0.091
	Rh–Ag_{ico} (av.)	0.254	0.219	0.190	0.168	0.151
	Ag_{ico}–Ag_{ico} (av.)	-	-	0.083	0.080	0.068
	Ag_{ico}–Ag_{cap} (av.)	-	-	0.052	0.047	0.042

significant hydride character were found at a rather low energy (~ 11 eV), and with some 5s/5p Rh admixture. This is the trace of a non-negligible participation of these latter AOs to the Rh-H bonding, contrarily to the case of $[PtHAg_{19}\{S_2P(O^nPr)_2\}_{12}]$,[13] in which Pt uses mainly its $5d_{z^2}$ AO for Pt-H bonding.

The NAO valence configuration of Rh in **1** is $4d^{9.28}\ 5s^{0.99}\ 5p^{0.36}$. Its central Ag counterpart in the hypothetical homometallic isoelectronic analog $[\{Ag@Ag_{21}\}(dtp)_{12}]^{2+}$ is $4d^{9.86}\ 5s^{1.06}\ 5p^{0.32}$. The substantial difference between the 4d(Rh) and 4d(Ag) populations of the central atoms in the two species indicates a non-negligible contribution of the 4d Rh AOs in the unoccupied 1D *superatomic* orbitals. However, this involvement is not enough important for **1** being considered as an 18-electron *superatom*.[38] The Rh NAO valence configuration in **2** and **3** is $4d^{9.28}\ 5s^{0.87}\ 5p^{0.33}$ and $4d^{9.25}\ 5s^{0.79}\ 5p^{0.31}$, respectively. Whereas the 4d population remains stable when going from **1** to **2** or **3**, the 5s and (to a lesser extent) 5p populations decrease somewhat, indicating significant participation of the latter AOs to Rh-H bonding. Thus, contrarily to Pt in $[PtHAg_{19}(dtp/dsep)_{12}]$,[13] the 5s AO of Rh in **2** and **3** is involved in the building of both Rh-H and *superatomic* bonding. This situation allows the H-atoms to somewhat also participate to *superatomic* bonding, in a larger extent as H in $[PtHAg_{19}(dtp/dsep)_{12}]$. In any case, the encapsulated hydride(s) provide(s) the central atom with the number of electrons required for the whole cluster, reaching the closed-shell 8-electron count. This peculiar behavior has been coined that of "metallic hydrogen",[39] as opposed to that of classical hydride ligands, whose electrons do not participate to the *superatomic* count.

DFT-modelling can also help in understanding the possible co-existence of isomers. For example, once fully optimized, the structure of minor contribution in the crystal of **1** (see above) was found to be only 1.1 kcal/mol less stable in Gibbs free energy than the structure analyzed above. Both isomers differ only by the position of two capping atoms and have similar electronic structures. Likewise, in the case of **2**, a C_3 isomer isostructural to $[PdHAg_{20}(dtp)_{12}]^+$[31] was found 1.8 kcal/mol more stable in Gibbs free energy that the structure analyzed above. In the case of **3**, an isomer of minor contribution in the crystal was found quasi-degenerate in free energy (and with H-Rh-H = 81°) with the structure described above. Another isomer, which can be described as a C_3-distorted structure (H-Rh-H = 136°) is found more stable in Gibbs free energy by 1.1 kcal/mol. These results are consistent with the possibility of existence of several isomers in solution and their easy interconversion by exchanging their Ag_{cap} atoms on their various available sites. Such a feature has been shown to be common within the family of silver-rich dichalcogenolate-protected 8-electron clusters.[31,36,40] It is also consistent with the ease of movement of the hydrides within their icosahedral cage, associated with an important flexibility of the H-Rh-H angle. This feature explains the fact that the optimized and experimental structures of **3** do not match perfectly with respect to the hydride positions.

The TD-DFT UV-Vis spectra simulated at the CAM-B3LYP/Def2-TZVP level (see Computational Details in the SI) of clusters **1**-**3** are shown in Figures S27-S28. The agreement with experiment is good for **1** and **2**. In the case of **3**, only one low energy band is present in the experimental spectrum, whereas it is split into two bands in the simulated spectrum. This (moderate) discrepancy can be tentatively attributed to the existence of several isomers in solution. The low-energy band in **1** and **2** is of mixed 1P→1D and 4d(Rh)→1D nature (Tables S4-45). The simulated band of lowest energy in **3** (435 nm) corresponds to 1P→1D transitions, whereas that at 361 nm has gained 4d(Rh)→1D character (Table S6). It is noteworthy that the 4d valence orbitals of the encapsulated Rh are involved in the transitions of lowest energy, contrary to their isoelectronic group 10- or 11-centered relatives.[9,13,16-17,19,31,36,38]

Conclusion

In summary, we successfully synthesized a $[RhH_x@Ag_{21-x}\{S_2P(O^nPr)_2\}_{12}]$ series of three 8-electron NCs: $[RhAg_{21}\{S_2P(O^nPr)_2\}_{12}]$ (**1**; x = 0), $[RhHAg_{20}\{S_2P(O^nPr)_2\}_{12}]$ (**2**; x = 1) and $[RhH_2Ag_{19}\{S_2P(O^nPr)_2\}_{12}]$ (**3**; x = 2), using the one-pot co-reduction method. Notably, compound **1** repre-

sents the first example of a hydride-free Rh-doped silver-rich superatom, with a regular Rh-centered Ag_{12} icosahedral kernel. As the number of interstitial hydrides increases, the icosahedron becomes more distorted. This study also reports the first observation of a three-coordinated hydride in **3** and a four-coordinated hydride in **2** and **3**, fully ascertained by neutron diffraction in Rh/Ag alloy NCs. All three NCs exhibit strong photoluminescence in the near-infrared region at 77K in 2-MeTHF glass. The property of **3** which easily releases H suggests that this cluster could be a good electrocatalyst for hydrogen evolution reaction (HER).[41, 42] This will be the subject of our future research on these compounds. This work highlights the impact of varying the number of "metallic hydrogens" encapsulated within the *superatomic* core.

ASSOCIATED CONTENT

Supporting Information. This material is available free of charge via the Internet at http://pubs.acs.org.

Experimental and computational details, X-ray and neutron structure analyses, NMR spectra data, XPS, ESI-MS, crystal and TLC image, luminescence decay curves (PDF)

Accession Codes

CCDC 2255283–2255287 contain the supplementary crystallographic data for this paper. These data can be obtained free of charge via www.ccdc.cam.ac.uk/data_request/cif, or by emailing data_request@ccdc.cam.ac.uk, or by contacting The Cambridge Crystallographic Data Centre, 12 Union Road, Cambridge CB2 1EZ, UK; fax: +44 1223 336033.

AUTHOR INFORMATION

Corresponding Author

C. W. Liu – Department of Chemistry, National Dong Hwa University, Shoufeng 97401, Taiwan, R.O.C.; orcid.org/ 0000-0003-0801-6499; Phone: +886-3-8903607; Email: chenwei@gms.ndhu.edu.tw ; Fax: +886-3-8900162

Jean-Yves Saillard – Univ Rennes, CNRS, F-35000 Rennes, France; orcid.org/0000-0003-4469-7922; Email: jean-yves.saillard@univ-rennes1.fr

Authors

Tzu-Hao Chiu – Department of Chemistry, National Dong Hwa University, Shoufeng 97401, Taiwan (R.O.C.)

Jian-Hong Liao – Department of Chemistry, National Dong Hwa University, Shoufeng 97401, Taiwan (R.O.C.)

Ying-Yann Wu – Department of Chemistry, National Dong Hwa University, Shoufeng 97401, Taiwan (R.O.C.)

Jie-Ying Chen - Department of Chemistry, Fu-Jen Catholic New Taipei City 24205, Taiwan (R.O.C.)

Yuan Jang Chen - Department of Chemistry, Fu-Jen Catholic New Taipei City 24205, Taiwan (R.O.C.)

Xiaoping Wang – Neutron Scattering Division, Neutron Sciences Directorate Oak Ridge National Laboratory, Oak Ridge, Tennessee 37831, United States; orcid.org/0000-0001- 7143-8112

Samia Kahlal – Univ Rennes, CNRS, F-35000 Rennes, France

Notes

The authors declare no competing financial interest.

ACKNOWLEDGMENT

This work was supported by the National Science and Technology Council of Taiwan (NSTC 111-2113-M-259-002) and the GENCI French National Computer Resource Center (A0030807367). We thank Dr. R. Marchal for its computational help. Single-crystal neutron diffraction performed on TOPAZ used resources at the Spallation Neutron Source, a DOE Office of Science User Facility operated by the Oak Ridge National Laboratory, under contract no. DE-AC05-00OR22725 with UT-Battelle, LLC. We thank the Instrumentation Center of National Taiwan Normal University (NSTC 111-2731-M-003-001), and Academia Sinica High-Field NMR Center (HFNMRC) for technical support; HFNMRC is funded by Academia Sinica Core Facility and Innovative Instrument Project (AS-CFII-111-214).

REFERENCES

1. Jin, R.; Zeng, C.; Zhou, M.; Chen, Y. Atomically Precise Colloidal Metal Nanoclusters and Nanoparticles: Fundamentals and Opportunities. *Chem. Rev.*, **2016**, *116,* 10346-10413.
2. Chakraborty, I.; Pradeep, T. Atomically Precise Clusters of Noble Metals: Emerging Link between Atoms and Nanoparticles. *Chem. Rev.*, **2017**, *117*, 8208-8271.
3. Du, Y.; Sheng, H.; Astruc, D.; Zhu, M. Atomically Precise Noble Metal Nanoclusters as Efficient Catalysts: A Bridge between Structure and Properties. *Chem. Rev.* **2020**, *2*, 526-622.
4. Maity, S.; Bain, D.; Patra, A. An overview on the current understanding of the photophysical properties of metal nanoclusters and their potential applications. *Nanoscale*, **2019**, *121*, 22685-22723.
5. Hirai, H.; Ito, S.; Takano, S.; Koyasu, K.; Tsukuda, T. Ligand-protected gold/silver superatoms: current status and emerging trends. *Chem. Sci.*, **2020**, *11*, 12233-12248.
6. Walter, M.; Akola, J.; Lopez-Acevedo, O.; Jadzinsky, P. D.; Calero, G.; Ackerson, C. J.; Whetten, R. L.; Grönbeck, H.; Häkkinen, H. A unified view of ligand-protected gold clustersas superatom complexes. *Proc. Natl. Acad. Sci. USA*, **2008**, *105*, 9157–9162.
7. Zhang, S.-S.; Feng, L.; Senanayake, R. D.; Aikens, C. M.; Wang, X.-P.; Zhao, Q.-Q.; Tung, C.-H.; Sun, D. Diphosphine-Protected Ultrasmall Gold Nanoclusters: Opened Icosahedral Au_{13} and Heart-Shaped Au_8 *Clusters. Chem. Sci.* **2018**, *9*, 1251-1258.
8. Shichibu, Y.; Konishi, K. HCl-Induced Nuclearity Convergence in Diphosphine-Protected Ultrasmall Gold Clusters: A Novel Synthetic Route to "Magic-Number" Au_{13} Clusters. *Small* **2010**, *6*, 1216-1220.
9. Dhayal, R. S.; Liao, J.-H.; Liu, Y.-C.; Chiang, M.-H.; Kahlal, S.; Saillard, J.-Y.; Liu, C. W. $[Ag_{21}\{S_2P(O^iPr)_2\}_{12}]^+$: An Eight-Electron Superatom. *Angew. Chem., Int. Ed.* **2015**, *54*, 3702-3706.
10. Joshi, C. P.; Bootharaju, M. S.; Alhilaly, M. J.; Bakr, O. M. $[Ag_{25}(SR)_{18}]^-$: The "Golden" Silver Nanoparticle. *J. Am. Chem. Soc.* **2015**, *137*, 11578-11581.
11. AbdulHalim, L. G.; Bootharaju, M. S.; Tang, Q.; del Gobbo, S.; AbdulHalim, R. G.; Eddaoudi, M.; Jiang, D.-e.; Bakr, O. M. $Ag_{29}(BDT)_{12}(TPP)_4$: A Tetravalent Nanocluster. *J. Am. Chem. Soc.* **2015**, *137*, 11970-11975.

12. Zhu, M.; Aikens, C. M.; Hollander, F. J.; Schatz, G. C.; Jin, R. Correlating the Crystal Structure of a Thiol-Protected Au_{25} Cluster and Optical Properties. *J. Am. Chem. Soc.* **2008**, *130*, 5883-5885.

13. Chiu, T.-Z.; Liao, J.-H.; Gam, F.; Wu, Y.-Y.; Wang, X.; Kahlal, S.; Saillard, J.-Y.; Liu, C.-W. Hydride-Containing Eight-Electron Pt/Ag Superatoms: Structure, Bonding, and Multi-NMR Studies. *J. Am. Chem. Soc.* **2022**, *144*, 10599-10607.

14. Yi, H.; Han, S. M.; Song, S.; Kim, M.; Sim, E.; Lee, D. Superatom-in-Superatom $[RhH@Ag_{24}(SPhMe_2)_{18}]^{2-}$ Nanocluster *Angew. Chem., Int. Ed.* **2021**, *60,* 22293-22300.

15. Yi, H.; Song, S.; Han, S. M.; Lee, J.; Kim, W.; Sim, E.; Lee, D. Superatom-in-Superatom Nanoclusters: Synthesis, Structure, and Photoluminescence *Angew. Chem., Int. Ed.* **2023**, *62*, e202302591.

16. Barik, S. K.; Chiu, T.-H.; Liu, Y.-C.; Chiang, M.-H.; Gam, F.; Chantrenne, I.; Kahlal, S.; Saillard, J.-Y.; Liu, C. W. Mono- and hexa-palladium doped silver nanoclusters stabilized by dithiolates. *Nanoscale* **2019**, *11*, 14581-14586.

17. Chiu, T.-H.; Liao, J.-H.; Gam, F.; Chantrenne, I.; Kahlal, S.; Saillard, J.-Y.; Liu, C. W. Homoleptic Platinum/Silver Superatoms Protected by Dithiolates: Linear Assemblies of Two and Three Centered Icosahedra Isolobal to Ne_2 and I_3^-. *J. Am. Chem. Soc.* **2019**, *141*, 12957-12961.

18. Chiu, T.-H.; Liao, J.-H.; Gam, F.; Chantrenne, I.; Kahlal, S.; Saillard, J.-Y.; Liu, C. W. All-selenolate-protected eight-electron platinum/silver nanoclusters. *Nanoscale* **2021**, *13*, 12143-12148.

19. Chang, W.-T.; Lee, P.-Y.; Liao, J.-H.; Chakrahari, K. K.; Kahlal, S.; Liu, Y.-C.; Chiang, M.-H.; Saillard, J.-Y.; Liu, C. W. Eight-Electron Silver and Mixed Gold/Silver Nanoclusters Stabilized by Selenium Donor Ligands. *Angew. Chem. Int. Ed.* **2017**, *56*, 10178-10182.

20. Liao, J.-H.; Kahlal, S.; Liu, Y.-C.; Chiang, M.-H.; Saillard, J.-Y.; Liu, C. W. Identification of an Eight-Electron Superatomic Cluster and Its Alloy in One Co-crystal Structure. *J. Clust. Sci.* **2018**, *29*, 827-835.

21. Kim, M.; Weerawardene, K. L. D. M.; Choi, W.; Han, S. H.; Paik, J.; Kim, Y.; Choi, M.-G.; Aikens, C. M.; Lee, D. Insights into the Metal-Exchange Synthesis of $MAg_{24}(SR)_{18}$ (M = Ni, Pd, Pt) Nanoclusters. *Chem. Mater.* **2020**, *32*, 10216-10226.

22. Yan, J.; Su, H.; Yang, H.; Malola, S.; Lin, S.; Hakkinen, H.; Zheng, N. Total Structure and Electronic Structure Analysis of Doped Thiolated Silver $[MAg_{24}(SR)_{18}]^{2-}$ (M = Pd, Pt) Clusters. *J. Am. Chem. Soc.* **2015**, *137*, 11880-11883.

23. Bootharaju, M. S.; Joshi, C. P.; Parida, M. R.; Mohammed, O. F.; Bakr, O. M. Templated Atom-Precise Galvanic Synthesis and Structure Elucidation of a $[Ag_{24}Au(SR)_{18}]^-$ Nanocluster. *Angew. Chem. Int. Ed.* **2015**, *55*, 922-926.

24. Kang, X.; Zhou, M.; Wang, S.; Sun, G.; Zhu, M.; Jin, R. The tetrahedral structure and luminescence properties of Bimetallic $Pt_1Ag_{28}(SR)_{18}(PPh_3)_4$ nanocluster. *Chem. Sci.* **2017**, *8*, 2581-2587.

25. Kang, X.; Huang, L.; Liu, W.; Xiong, L.; Pei, Y.; Sun, Z.; Wang, S.; Wei, S.; Zhu, M. Reversible nanocluster structure transformation between face-centered cubic and icosahedral isomers. *Chem. Sci.* **2019**, *10*, 8685-8693.

26. Hirai, H.; Takano, S.; Nakamura, T.; Tsukuda, T. Understanding Doping Effects on Electronic Structures of Gold Superatoms: A Case Study of Diphosphine-Protected $M@Au_{12}$ (M = Au, Pt, Ir). *Inorg. Chem.* **2020**, *59*, 17889-17895.

27. Takano, S.; Hirai, H.; Nakashima, T.; Iwasa, T.; Taketsugu, T.; Tsukuda, T. Photoluminescence of Doped Superatoms $M@Au_{12}$ (M = Ru, Rh, Ir) Homoleptically Capped by $(Ph_2)PCH_2P(Ph_2)$: Efficient Room-Temperature Phosphorescence from $Ru@Au_{12}$. *J. Am. Chem. Soc.* **2021**, *143,* 10560-10564.

28. Hirai, H.; Takano, S.; Nakamura, T.; Iwasa, T.; Taketsugu, T.; Tsukuda, T. Doping-Mediated Energy-Level Engineering of $M@Au_{12}$ Superatoms (M=Pd, Pt, Rh, Ir) for Efficient Photoluminescence and Photocatalysis. *Angew. Chem. Int. Ed.* **2022**, *134*, e202207290.

29. Hirai, H.; Nakashima, T.; Takano, S.; Shichibu, Y.; Konishi, K.; Kawai, T.; Tsukuda, T. $IrAu_{12}$ superatom modified by chiral diphosphines: doping-induced enhancement of chiroptical activity. *J. Mater. Chem. C* **2023**, *11*, 3095-3100.